Radiogenomics-Driven Hierarchical Multimodal Stacking for Non-Invasive Triage of High-Risk PKD1-Truncating Genotypes in ADPKD

Oybek Valiyev[1], JunBeom Cho[1], and Youngwoo Kim[1,2*]

[1] Department of Software Engineering,[2] Department of Computer Engineering; Kumoh National Institute of Technology, Gumi, 39177, Republic of Korea
oybek07valiyev@gmail.com, jjb6065@naver.com, ywkim09@gmail.com

Abstract. Autosomal dominant polycystic kidney disease (ADPKD) exhibits a pronounced genotype-phenotype gap and substantial radiological "biological mimicry" across mutation classes, which together hinder early risk stratification. Height-adjusted total kidney volume (htTKV) is the current gold-standard imaging biomarker for disease progression, yet its ability to resolve underlying genetic subtypes is limited by extensive phenotype overlap. In particular, high-risk PKD1-truncating (PKD1-T) mutations are often radiologically indistinguishable from milder PKD1 non-truncation (PKD1-NT), PKD2, or no-mutation-detected cases on routine MRI. This work introduces a radiogenomics-driven, two-stage hierarchical stacking framework that integrates 3D MRI radiomics with clinical profiles for non-invasive triage of PKD1-T genotypes. First, handcrafted radiomic features are extracted from automatically segmented total kidney volume masks on T2-weighted MRI and compressed into out-of-fold (OOF) probabilistic representations using multiple base classifiers under strictly nested cross-validation. These compact radiomics-derived signatures are then fused with clinical variables (age, htTKV) in a meta-learning stage designed to capture non-linear imaging-clinical interactions while rigorously preventing data leakage. On a multi-institutional cohort of 414 genetically confirmed ADPKD patients, the proposed hierarchical multimodal framework achieves an AUC of 0.722 ± 0.060 and an accuracy of 0.725 ± 0.058 for discriminating PKD1-T from a heterogeneous "Other PKD" group, significantly outperforming both radiomics-only (AUC 0.677 ± 0.061) and clinical-only (AUC 0.664 ± 0.081) baselines. These findings highlight the complementary value of 3D MR-based radiomic texture heterogeneity and tabular clinical profiles for non-invasive radiogenomic triage of high-risk PKD1-T genotypes, particularly where comprehensive genetic testing is limited by cost or availability.

Keywords: Autosomal dominant polycystic kidney disease· Radiomics· Radiogenomics· Genotype classification· Hierarchical stacking.

* Corresponding author

1 Introduction

Autosomal Dominant Polycystic Kidney Disease (ADPKD) is a prevalent hereditary chronic kidney disease characterized by progressive bilateral renal cyst formation leading to renal impairment and frequently end-stage renal disease (ESRD) [1,2]. It affects approximately 12.5 million individuals worldwide (prevalence ∼1:1000) and accounts for 5–10% of ESRD cases [1–3]. Beyond renal failure, ADPKD is associated with systemic complications, including early-onset hypertension, polycystic liver disease, and cerebral aneurysms [4]. The genetic architecture of ADPKD is dominated by mutations in the PKD1 and PKD2 genes, encoding polycystin-1 and polycystin-2, respectively [5, 6]. Approximately 78% of cases are attributed to PKD1 mutations and 15% to PKD2, while the remainder are genetically unresolved or involve rarer genes such as IFT140, GANAB, DNAJB11, and ALG9 [7–9]. Disease severity is highly heterogeneous: PKD1 mutations, particularly truncating variants, are associated with a more aggressive phenotype and earlier ESRD onset (54.3-55.6 years), whereas PKD2 mutations present with milder disease and delayed ESRD (79.7 years) [10–12].

A central challenge in ADPKD management is the pronounced genotype–phenotype discordance, which severely limits early risk individualized therapy. Height-adjusted total kidney volume (htTKV) is an established prognostic biomarker and underpins the Mayo Imaging Classification (MIC); however, it is intrinsically limited in discriminating genetic subtypes due to substantial radiologic overlap ("biological mimicry") across mutation classes. Patients with distinct genotypes (e.g., aggressive PKD1-T vs. milder PKD1-NT or PKD2) frequently fall within the same MIC categories, resulting in suboptimal genetic triage [13].

Prior machine learning studies in ADPKD imaging have primarily focused on binary classification tasks, such as PKD1 versus PKD2 discrimination or MIC risk stratification [14]. While these works demonstrate the promise of quantitative texture analysis and radiomics, they largely overlook the clinically more demanding intra-PKD1 heterogeneity—specifically, isolating high-risk PKD1-T mutations from a heterogeneous "Other PKD" group that includes PKD1-NT, PKD2-truncating (PKD2-T), PKD2-non-truncating (PKD2-NT), and no-mutation-detected (NMD) cases. This diagnostic gap is particularly accurate for PKD1-NT variants, which exhibit intermediate phenotypes that closely mimic less aggressive forms on conventional MRI [15]. This convergence of imaging appearances across distinct genotypes can be viewed as radiological biological mimicry, where standard imaging and coarse volumetric markers fail to capture 3D textural and morphological signatures linked to high-risk genotypes. A similar phenomenon has been extensively documented in oncology, where molecularly distinct tumor subtypes share overlapping radiologic phenotypes, motivating the use of high-dimensional radiomics and radiogenomics to uncover latent imaging signatures [16]. In ADPKD, multimodal radiomics–clinical nomograms have shown potential for renal function assessment and risk prediction, yet there remains a lack of frameworks specifically tailored for the non-invasive triage of PKD1-T genotypes that (1) explicitly model non-linear interactions between

high-dimensional radiomics and clinical profiles and (2) rigorously prevent data leakage [17].

In this work, a two-stage hierarchical stacking framework is proposed to address these gaps. The approach focuses on discriminating PKD1-T mutations from phenotypically overlapping "Other PKD" genotypes in a multi-institutional cohort of 414 genetically confirmed ADPKD patients. By combining 3D MRI-derived radiomic signatures with routine clinical variables within a strictly nested cross-validation paradigm, the framework aims to mitigate radiological mimicry and enhance non-invasive genotype stratification. The main contributions of this study are as follows:

- **Hierarchical multimodal fusion:** A two-stage stacking architecture is introduced to integrate compact out-of-fold (OOF) radiomics-derived representations with structured clinical profiles, allowing the meta-learner to capture complex, non-linear imaging-clinical interactions while controlling overfitting.
- **High-risk genotype triage:** The framework is explicitly tailored to clinically critical task of isolating high-risk PKD1-T mutations from heterogeneous "Other PKD" group, addressing an unmet need beyond conventional PKD1 versus PKD2 or MIC risk classification.
- **Multi-institutional validation:** Evaluation on a multi-institutional cohort of 414 genetically confirmed ADPKD patients after quality control demonstrates improved discrimination, calibration, and decision-analytic net benefit, suggesting potential integration into clinical decision support pipelines.

2 Methodology

2.1 Dataset and Radiomics Features Extraction

This retrospective multi-institutional study included 3D T2-weighted MRI and genetic profiles from 478 patients with clinically diagnosed ADPKD, drawn from the HALT-PKD study cohort whose design, recruitment, and ethics approvals are described previously [18,19]; as secondary analysis of fully de-identified data, additional Institutional Review Board review and written informed consent were waived. After quality control, 414 cases were retained for analysis. Based on genetic testing, patients were categorized into five mutation types as described in the Introduction. For the primary binary classification task, cases were grouped into a high-risk PKD1-T cohort ($n = 197$, mean age 33.6 ± 8.3 years) and a composite "Other PKD" cohort ($n = 217$, mean age 37.6 ± 7.8 years), comprising PKD1-NT ($n = 118$), PKD2-T ($n = 57$), PKD2-NT ($n = 14$), and NMD ($n = 28$) variants.

Automated Segmentation. The region of interest (ROI) was defined as the total kidney volume (TKV). Baseline T2-weighted MR images were segmented using a pretrained nnU-Net-based segmentation framework to generate bilateral kidney and cyst masks for subsequent radiomics analysis [20].

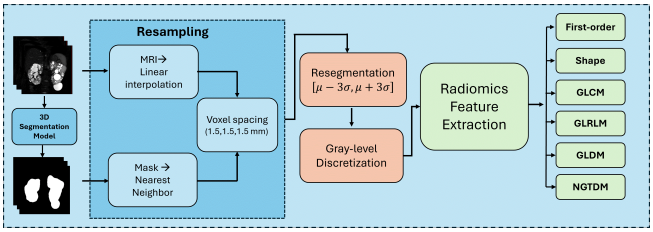

Fig. 1. Radiomics feature extraction pipeline from automatically segmented total kidney volume masks.

Pre-processing and Feature Extraction. Image pre-processing followed IBSI guidelines [21]. Images and masks were resampled to an isotropic resolution of $1.5 \times 1.5 \times 1.5$ mm^3. Voxel intensities within the TKV were clipped to $[\mu - 3\sigma, \mu + 3\sigma]$ to reduce noise while preserving subject-specific distributions.

Intensity discretization was performed using a fixed bin width of 25, consistent with PyRadiomics defaults and prior renal radiomics work [22]. Radiomic features were extracted using PyRadiomics v3.0 with IBSI-compliant settings (no filtering; original features only) [23]. A total of 107 handcrafted features were computed, including 14 shape descriptors, 18 first-order intensity features, and 75 texture features (GLCM, GLRLM, GLSZM, NGTDM, and GLDM), to capture 3D morphological and textural differences between PKD1-T and other genotypes (Fig. 1).

2.2 Feature Selection

To address the curse of dimensionality inherent in high-dimensional radiomics and to enhance model generalizability, feature selection was implemented in a strictly nested manner within each outer cross-validation fold, ensuring strict separation of training and test data. Radiomic features were first normalized using robust scaling based on the inter-quartile range (IQR), with scaling parameters estimated solely from the outer training data and applied unchanged to the corresponding held-out test fold. Dimensionality reduction was performed using the Least Absolute Shrinkage and Selection Operator (LASSO), an embedded regularization method well-suited for correlated radiomics features. The LASSO objective is given by

$$\min_{\boldsymbol{\beta}} \left\{ \frac{1}{2n} \sum_{i=1}^{n} \left(y_i - \mathbf{x}_i^\top \boldsymbol{\beta} \right)^2 + \lambda \sum_{j=1}^{p} |\beta_j| \right\}, \tag{1}$$

where n is the number of samples, p is the number of features, $\mathbf{x}_i$ and y_i denote the feature vector and label for sample i, and λ controls the sparsity of the coefficient vector β. The regularization parameter λ was optimized within each outer training fold using an inner 5-fold stratified cross-validation loop, selecting

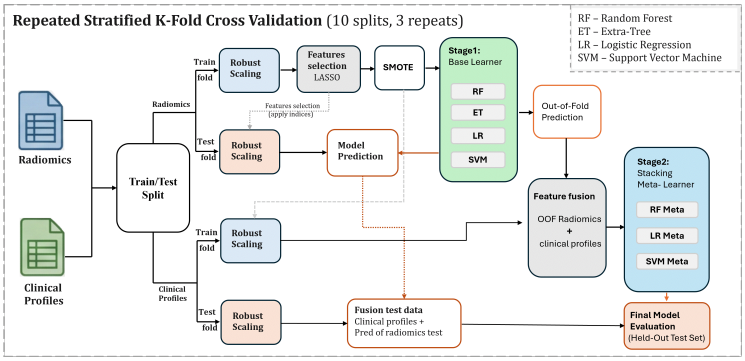

Fig. 2. Overview of the proposed two-stage multimodal stacking framework integrating radiomics and clinical profiles under nested cross-validation.

the value that minimized the mean squared error. Features with non-zero coefficients were retained, and the selected feature subset was fixed and applied to the held-out test fold without re-estimation. Feature selection was restricted to radiomics due to their high dimensionality, while clinical profiles were retained unchanged. Class imbalance was addressed using SMOTE, applied exclusively within the training data of each outer fold to prevent data leakage.

2.3 Hierarchical Stacking Framework

A two-stage hierarchical stacking framework was designed to integrate radiomics-derived representations with clinical profiles while rigorously preventing data leakage (Fig. 2). The entire pipeline was implemented under a repeated stratified 10-fold cross-validation scheme with three repeats, yielding 30 outer test partitions. A late-fusion strategy was adopted to avoid dominance of high-dimensional radiomic features over low-dimensional clinical variables and to preserve modality-specific information.

Stage 1: Base-Level Radiomics Modeling. Within each training fold of the outer cross-validation loop, radiomic features underwent robust scaling and LASSO-based selection as described in Section 2.2. The selected feature subset was then applied to the corresponding outer test fold. SMOTE was used only on the training data after feature selection to mitigate class imbalance. Multiple base learners, including Random Forest (RF), Extra Trees (ET), Logistic Regression (LR), and Support Vector Machine (SVM), were trained on the selected radiomic features. Out-of-fold (OOF) probability predictions were obtained via inner cross-validation. These OOF predictions constitute compact radiomics-derived representations for each base model, which are concatenated to form a low-dimensional radiomics signature that is passed to the meta-learning stage.

Stage 2: Hybrid Meta-Classification. A hybrid meta-feature space was constructed by fusing the Stage-1 radiomics OOF predictions (for each base

learner) with clinical variables (age, htTKV). Clinical features were normalized per outer fold using training-only statistics. Meta-learners (RF, LR, and SVM) were trained solely on this fused feature space to capture non-linear interactions between imaging-derived signatures and clinical profiles. Decision thresholds were optimized by maximizing the Youden index on training ROC curves within each outer fold. Final performance metrics were computed by aggregating predictions on the held-out test subjects across all outer folds and repeats.

2.4 Statistical Analysis

For all models, performance metrics-including area under the ROC curve (AUC), accuracy, F1-score, sensitivity, and specificity were reported as mean ± standard deviation across the 30 outer test folds (3 repeats × 10 folds). To assess the significance of improvements over unimodal baselines, two-sided Wilcoxon signed-rank tests were conducted on paired test-fold results ($n = 30$), explicitly accounting for dependencies inherent in repeated cross-validation partitions. A p-value < 0.05 was considered statistically significant. Calibration quality was evaluated using calibration curves and Expected Calibration Error (ECE). Clinical utility was assessed via Decision Curve Analysis (DCA), which compares the net benefit of different models across a range of clinically plausible threshold probabilities for classifying PKD1-T versus Other PKD.

3 Results

Overall Classification Performance. Table 1 summarizes the classification performance of clinical-only, radiomics-only, and multimodal models, with ROC curves shown in Fig. 4a. The multimodal Hybrid RF meta-classifier achieved the highest discrimination (AUC 0.722 ± 0.060; accuracy 0.725 ± 0.058), significantly outperforming both the radiomics-only baseline (AUC 0.677 ± 0.061, $p = 0.001$) and the clinical-only baseline (AUC 0.664 ± 0.081, $p < 0.001$).

Table 1. Performance comparison across modalities and hybrid strategies: (a) clinical-only meta-models, (b) radiomics only meta-models, (c) combined radiomics and clinical profiles.

	Model	AUC	Accuracy	F1-score	Sensitivity	Specificity
(a)	RF Meta	0.664 ± 0.081	0.680 ± 0.065	0.665 ± 0.113	0.709 ± 0.197	0.652 ± 0.202
	LR Meta	0.647 ± 0.084	0.675 ± 0.061	0.650 ± 0.107	0.669 ± 0.183	0.681 ± 0.190
	SVM Meta	0.659 ± 0.088	0.684 ± 0.070	0.664 ± 0.097	0.685 ± 0.181	0.683 ± 0.193
(b)	RF Meta	0.677 ± 0.061	0.689 ± 0.053	0.703 ± 0.063	0.764 ± 0.142	0.602 ± 0.178
	LR Meta	0.675 ± 0.071	0.684 ± 0.054	0.698 ± 0.053	0.756 ± 0.162	0.591 ± 0.204
	SVM Meta	0.672 ± 0.069	0.692 ± 0.057	0.694 ± 0.073	0.755 ± 0.166	0.635 ± 0.181
(c)	RF Meta	$\mathbf{0.722 \pm 0.060}$	$\mathbf{0.725 \pm 0.058}$	$\mathbf{0.715 \pm 0.067}$	0.745 ± 0.150	0.706 ± 0.135
	LR Meta	0.705 ± 0.070	0.706 ± 0.057	0.710 ± 0.074	0.782 ± 0.163	0.638 ± 0.157
	SVM Meta	0.678 ± 0.073	0.689 ± 0.058	0.655 ± 0.080	0.657 ± 0.190	0.720 ± 0.164

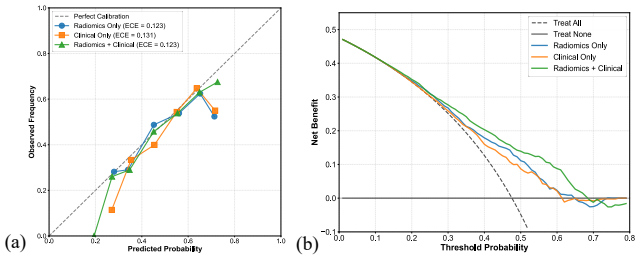

Fig. 3. Model validation and clinical utility. (a) Calibration curves with Expected Calibration Error (ECE) for clinical-only and multimodal models. (b) Decision Curve Analysis (DCA) demonstrating superior net benefit of the combined radiomics and clinical model across clinically relevant threshold probabilities.

No statistically significant difference was observed between the two unimodal strategies ($p > 0.05$). Notably, the multimodal framework yielded a more balanced diagnostic profile. While radiomics-only models tended to favor sensitivity at the expense of specificity, the Hybrid RF meta-classifier maintained high sensitivity (0.745 ± 0.150) and improved specificity to 0.706 ± 0.135, thereby reducing the rate of false positives compared to the radiomics-only baseline.

Calibration and Clinical Utility. Calibration analysis demonstrated improved probabilistic reliability for the multimodal model. As shown in Fig. 3a, the integrated Hybrid RF meta-classifier achieved a lower ECE (0.123) compared to the best clinical-only baseline (ECE = 0.131), with calibration curves closer to the ideal diagonal. DCA further supported the potential clinical benefit of multimodal integration. Across a range of threshold probabilities between 0.2 and 0.7, the multimodal model consistently provided higher net benefit than both radiomics-only and clinical-only models (Fig. 3b), indicating that it can reduce unnecessary interventions while preserving detection of high-risk PKD1-T patients in realistic decision-making scenarios.

Feature Contributions and Interpretability. SHAP analysis of the multimodal Hybrid RF meta-classifier identified baseline age as the most influential clinical predictor (Fig. 4b), consistent with established genotype–phenotype relationships in ADPKD. Within the radiomics domain, texture descriptors–particularly GLCM inverse difference (Id) and GLSZM Small Area Emphasis–exhibited the strongest contributions to model predictions. These metrics reflect fine-scale texture heterogeneity and small-scale cystic structure distribution within the TKV, suggesting that 3D MRI-derived texture patterns provide complementary information beyond htTKV for distinguishing PKD1-T from similar genotypes.

4 Discussion

This study addresses a clinically important but underexplored problem in ADPKD imaging: non-invasive triage of high-risk PKD1-T genotypes despite genotype–

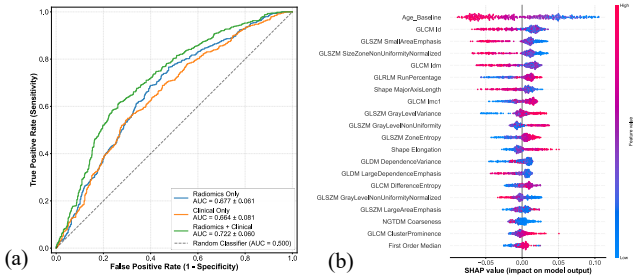

Fig. 4. Performance and interpretability. (a) ROC curves comparing clinical-only, radiomics-only, and multimodal models, (b) SHAP summary plot highlighting the most influential clinical and radiomic features for PKD1-T classification.

phenotype overlap. Unlike prior radiomics work that has mainly focused on PKD1 versus PKD2 discrimination, Mayo risk stratification, or renal function decline, the present framework targets the more challenging task of distinguishing PKD1-T from a heterogeneous "Other PKD" group [14]. This setting is particularly confounded by PKD1-NT variants, whose intermediate phenotype mimics less aggressive genotypes on conventional MRI and limits the separability of imaging signatures even under optimal modeling. Accordingly, the results should be interpreted as binary PKD1-T triage against the remaining ADPKD population, rather than subtype-level discrimination among PKD1-NT, PKD2-T, PKD2-NT, and other genotypes. In this biologically constrained context, a performance ceiling exists for imaging-based or radiomics-driven approaches, as MRI–genotype coupling is intrinsically weaker than in classic prognostic tasks. Consequently, mid-0.7 AUC values should be interpreted as competitive rather than modest, under multi-institutional evaluation with nested cross-validation.

The proposed framework improves over unimodal baselines by compressing high-dimensional radiomics into OOF probability signatures and then fusing them with clinical variables. This design yields not only higher AUC but also better sensitivity–specificity balance, improved calibration, and decision-analytic net benefit–key requirements for practical triage tools. Clinically, the model is intended as a non-invasive decision-support tool, not a replacement for genetic testing, to prioritize patients for earlier genetic evaluation, closer monitoring, or specialist referral when testing is unavailable, delayed, or costly.

Interpretability analyses support the radiogenomic rationale: age was the dominant clinical predictor, while GLCM- and GLSZM-based texture features contributed substantially to PKD1-T discrimination. Given the age-dependent nature of ADPKD imaging phenotypes, the dominant role of age may reflect both disease progression and residual confounding; nevertheless, the fused multimodal model outperformed the clinical-variable model, suggesting that prediction was not explained by age and htTKV alone. These findings indicate that 3D MRI-derived texture heterogeneity captures genotype-linked morphological patterns beyond htTKV alone, in line with broader radiogenomics findings in oncology.

However, the dominant SHAP contribution of age remains an important limitation, and future age-stratified or adjusted analyses are needed to better separate genotype-related imaging signals from age-related disease progression. Future work should include external hold-out validation, integration of multi-parametric MRI, incorporation of non-cystic parenchymal radiomics, segmentation sensitivity analysis using alternative or perturbed masks, and translation into simplified risk scores or nomograms to facilitate clinical deployment.

5 Conclusion

A hierarchical two-stage stacking framework integrating 3D MRI-based radiomics with clinical profiles can partially mitigate genotype–phenotype overlap in ADPKD and improve non-invasive identification of high-risk PKD1-T genotypes. Under rigorously nested validation, the multimodal model outperforms unimodal baselines in discrimination, calibration, and clinical net benefit using only standard-of-care MRI and routine clinical data. These results support multimodal radiogenomic profiling as a practical triage strategy for prioritizing genetic testing and closer surveillance, especially where sequencing is limited by cost or availability.

Acknowledgments. This work was supported by the National Research Foundation of Korea (NRF) grant funded by the Korean government (MSIT) (No. RS-2024-00345567) and the Korea Health Technology R&D Project through the Korea Health Industry Development Institute (KHIDI), funded by the Ministry of Health & Welfare, Republic of Korea (grant number : RS-2026-25541079).

Disclosure of Interests. The authors have no competing interests to declare that are relevant to the content of this article.

References

1. K. Burgmaier, C. Gimpel, F. Schaefer, and M. Liebau. Autosomal recessive polycystic kidney disease – pkhd1. In M. P. Adam, J. Feldman, G. M. Mirzaa, R. A. Pagon, S. E. Wallace, and A. Amemiya, editors, *GeneReviews®*. University of Washington, Seattle, Seattle (WA), 1993.
2. A. AlSahow. Renal data from the arab world: Dialysis in kuwait 2013–2019. *Saudi Journal of Kidney Diseases and Transplantation*, 31(4):826–830, 2020.
3. H. Ali. The genetic landscape of autosomal dominant polycystic kidney disease in kuwait. *Clinical Kidney Journal*, 16(2):355–366, 2023.
4. R. L. Luciano and N. K. Dahl. Extra-renal manifestations of autosomal dominant polycystic kidney disease (adpkd): Considerations for routine screening and management. *Nephrology Dialysis Transplantation*, 29(2):247–254, 2014.
5. C. M. Heyer. Predicted mutation strength of nontruncating pkd1 mutations aids genotype-phenotype correlations in autosomal dominant polycystic kidney disease. *Journal of the American Society of Nephrology*, 27(9):2872, 2016.

6. K. Hopp. Detection and characterization of mosaicism in autosomal dominant polycystic kidney disease. *Kidney International*, 97(2):370–382, 2020.
7. B. Porath. Mutations in ganab, encoding the glucosidase iiα subunit, cause autosomal-dominant polycystic kidney and liver disease. *American Journal of Human Genetics*, 98(6):1193–1207, 2016.
8. W. Besse. Alg9 mutation carriers develop kidney and liver cysts. *Journal of the American Society of Nephrology*, 30(11):2091–2102, 2019.
9. E. Cornec-Le Gall. Monoallelic mutations to dnajb11 cause atypical autosomal-dominant polycystic kidney disease. *American Journal of Human Genetics*, 102(5):832–844, 2018.
10. N. Hateboer. Comparison of phenotypes of polycystic kidney disease types 1 and 2. *The Lancet*, 353(9147):103–107, 1999.
11. P. C. Harris and K. Hopp. The mutation, a key determinant of phenotype in adpkd. *Journal of the American Society of Nephrology*, 24(6):868, 2013.
12. E. Cornec-Le Gall, V. E. Torres, and P. C. Harris. Genetic complexity of autosomal dominant polycystic kidney and liver diseases. *Journal of the American Society of Nephrology*, 29(1):13–23, 2018.
13. M. V. Irazabal. Imaging classification of autosomal dominant polycystic kidney disease: A simple model for selecting patients for clinical trials. *Journal of the American Society of Nephrology*, 26(1):160–172, 2015.
14. L. E. Kremer, A. B. Chapman, and S. G. Armato. Magnetic resonance imaging preprocessing and radiomic features for classification of autosomal dominant polycystic kidney disease genotype. *Journal of Medical Imaging*, 10(6):064503, 2023.
15. E. Cornec-Le Gall. Type of pkd1 mutation influences renal outcome in adpkd. *Journal of the American Society of Nephrology*, 24(6):1006–1013, 2013.
16. S. Yamamoto. Breast cancer: Radiogenomic biomarker reveals associations among dynamic contrast-enhanced mr imaging, long noncoding rna, and metastasis. *Radiology*, 275(2):384–392, 2015.
17. X. Li. A mri-based radiomics nomogram for evaluation of renal function in adpkd. *Abdominal Radiology*, 47(4):1385–1395, 2022.
18. A. B. Chapman et al. The HALT polycystic kidney disease trials: design and implementation. *Clinical Journal of the American Society of Nephrology*, 5(1):102–109, January 2010.
19. R. W. Schrier et al. Blood pressure in early autosomal dominant polycystic kidney disease. *New England Journal of Medicine*, 371(24):2255–2266, December 2014.
20. Y. Kim, C. Tao, H. Kim, G.-Y. Oh, J. Ko, and K. T. Bae. A deep learning approach for automated segmentation of kidneys and exophytic cysts in individuals with autosomal dominant polycystic kidney disease. *Journal of the American Society of Nephrology*, 33(8):1581–1589, 2022.
21. A. Zwanenburg. The image biomarker standardization initiative: Standardized quantitative radiomics for high-throughput image-based phenotyping. *Radiology*, 295(2):328–338, 2020.
22. Y. Han. The value of radiomics based on 2-[18f] fdg pet/ct in predicting who/isup grade of clear cell renal cell carcinoma. *EJNMMI Research*, 14:115, 2024.
23. J. J. M. van Griethuysen. Computational radiomics system to decode the radiographic phenotype. *Cancer Research*, 77(21):e104–e107, 2017.